

Bifurcation analysis of two-dimensional Rayleigh–Bénard convection

N. Boullé,* V. Dallas,† and P. E. Farrell‡

Mathematical Institute, University of Oxford, Woodstock Road, Oxford OX2 6GG, UK

(Dated: June 11, 2022)

We perform a bifurcation analysis of the steady state solutions of Rayleigh–Bénard convection with no-slip boundary conditions in two dimensions using a numerical method called deflated continuation. By combining this method with an initialisation strategy based on the eigenmodes of the conducting state, we are able to discover multiple solutions to this non-linear problem, including disconnected branches of the bifurcation diagram, without the need of any prior knowledge of the dynamics. One of the disconnected branches we find contains a s-shape bifurcation with hysteresis, which is the origin of the flow pattern that may be related to the dynamics of flow reversals in the turbulent regime. Linear stability analysis is also performed to analyse the steady and unsteady regimes of the solutions in the parameter space and to characterise the type of instabilities.

I. INTRODUCTION

This paper focuses on the bifurcations of the two-dimensional Rayleigh–Bénard convection, which supports a profusion of states. There have been numerous investigations trying to visualise solutions and characterise the steady-states of Rayleigh–Bénard convection, as well as computing its bifurcation diagrams with respect to Ra , the Rayleigh number, in various settings and for different geometries [1, 2]. Ouertatani et al. [3] performed numerical simulations of Rayleigh–Bénard convection in a square cavity using the finite volume method and computed fluid flow profiles and temperature patterns at $Ra = 10^4, 10^5, 10^6$. Numerical studies have been conducted to understand the existence of bifurcating solutions to this problem in a two-dimensional domain with periodic boundary conditions in the horizontal direction [4, 5]. Mishra et al. [6] analysed the effect of low Prandtl number on the bifurcation structures, while Peterson [7] used arclength continuation [8] to study the evolution of cell solutions with respect to the aspect ratio of the domain. Bifurcation structures of Rayleigh–Bénard convection have been extensively studied in cylindrical geometry by Ma et al. [9] as well as by Borońska and Tuckerman [10, 11]. In particular, references [10, 11] adapted a time-dependent code to perform branch continuation and they analysed the linear stability of the computed solutions using Arnoldi iterations [12]. Finally, Puigjaner et al. [13, 14] computed bifurcation diagrams for Rayleigh–Bénard convection in a cubical cavity over different intervals of $Ra < 1.5 \times 10^5$.

A common way to reconstruct bifurcation diagrams is to use arclength continuation and branch switching techniques [8, 15, 16] to continue known solutions in a given parameter. These solutions can be computed by applying Newton’s method to suitably chosen initial guesses or by using time-evolution algorithms. Then, a standard numerical technique in fluid dynamics for finding initial states for the continuation algorithm is to perform time-dependent simulation of initial solutions until a steady-state is reached [17–19]. These numerical techniques have been widely used and extremely successful at computing bifurcation diagrams of nonlinear PDEs.

In this paper, we employ a recent algorithm called deflation for computing multiple solutions to nonlinear partial differential equations [20, 21], which has been successfully applied to compute bifurcations to a wide range of physical problems such as the deformation of a hyperelastic beam [21], Carrier’s problem [22], cholesteric liquid crystals [23], and the nonlinear Schrödinger equation in two and three dimensions [24–26]. We emphasise that deflated continuation and its extensions offer some advantages that could be combined with the standard bifurcation analysis tools. The main strength of deflation is that it allows the detection of disconnected branches, in addition to those connected to known branches. An additional advantage is that it does not require the solution of augmented problems to find new solutions. Using perturbed solutions to the linearised equations as initial conditions, we are able to discover numerous steady-states solutions of Rayleigh–Bénard convection. These solutions can be obtained without the need of prior knowledge of the dynamics and regardless of the stability of the solutions.

While much progress in fluid dynamics has been made on the study of hydrodynamic instabilities, instabilities that occur when a control parameter is varied within the turbulent regime remain poorly understood [27]. The difficulty in studying such transitions arises from the underlying turbulent fluctuations which make analytical approaches cumbersome. These types of transitions resemble more closely phase transitions in statistical mechanics because the instability occurs on a fluctuating background [28]. In Rayleigh–Bénard convection, such transitions have been

* Email: nicolas.boullé@maths.ox.ac.uk

† Email: vassilios.dallas@maths.ox.ac.uk

‡ Email: patrick.farrell@maths.ox.ac.uk

observed in the form of reversals of the large scale circulation in an enclosed rectangular geometry, both in experiments and numerical simulations [29–31]. We therefore investigate the bifurcations of Rayleigh–Bénard convection in an enclosed rectangular geometry to attempt to understand the genesis of the flow patterns that play the central role in flow reversals in the turbulent regime.

The paper is organised as follows. We first discuss the problem set-up and the choice of parameters in Section II. Then, in Section III, we briefly review deflated continuation and present the methods used to improve its initialisation procedure and compute the linear stability of the solutions. Next, we analyse the different branches discovered by deflation and their stability in Section IV. Finally, in Section V, we recapitulate the main conclusions of this study and propose potential extensions for future work.

II. PROBLEM SET-UP

We consider Rayleigh–Bénard convection [32–34] of a confined fluid heated from below and maintained at a constant temperature difference $\Delta T = T - T_0$ across a two dimensional square cell of height d . For simplicity, we employ the Oberbeck–Boussinesq approximation [35–37] in which the kinematic viscosity ν and the thermal diffusivity κ do not depend on temperature while the fluid density ρ is assumed to be constant except in the buoyancy term of the momentum equation. In this case, we assume the density to depend linearly on the temperature, $\rho(T) \simeq \rho(T_0)[1 - \alpha\Delta T]$, where α is the thermal expansion coefficient. Then, the governing equations of the problem are

$$\nabla \cdot \mathbf{u} = 0, \quad (1a)$$

$$\partial_t \mathbf{u} + \mathbf{u} \cdot \nabla \mathbf{u} = -\nabla p + Pr \nabla^2 \mathbf{u} + Pr Ra T \hat{\mathbf{z}}, \quad (1b)$$

$$\partial_t T + \mathbf{u} \cdot \nabla T = \nabla^2 T, \quad (1c)$$

where \mathbf{u} is the velocity field, T is the temperature field, p is the pressure, and $\hat{\mathbf{z}}$ is the buoyancy direction. The above equations have been nondimensionalized using d , d^2/κ and ΔT as the relevant scales for length, time and temperature, respectively. The two dimensionless parameters of the problem are the Rayleigh and Prandtl numbers

$$Ra = g\alpha\Delta T d^3 / (\nu\kappa), \quad Pr = \nu/\kappa, \quad (2)$$

where g is the gravitational acceleration. The Rayleigh number represents the ratio of the acceleration $g\alpha\Delta T$ related to buoyancy to the stabilizing effects of ν and κ . The bifurcation parameter in the problem we study is Ra by fixing $Pr = 1$. The cell is assumed to have rigid walls, with thermally conducting horizontal walls and thermally insulating side walls, i.e.

$$u = w = 0, \quad x = z = 0, 1, \quad (3a)$$

$$T = 1, \quad z = 0, \quad (3b)$$

$$T = 0, \quad z = 1, \quad (3c)$$

$$\partial_x T = 0, \quad x = 0, 1. \quad (3d)$$

The trivial steady state solution is a motionless state with a negative thermal gradient upwards through the layer

$$\mathbf{u} = 0, \quad T = 1 - z, \quad (4)$$

called conducting state. This is because the fluid acts as a conducting material. The cooler fluid near the top of the layer is denser than the warmer fluid underneath it. The classical stability analysis on this steady state for a critical value of the Rayleigh number Ra_c reveals the well-known Rayleigh–Bénard cellular instability which gives a pattern of two counter-rotating convection rolls. Note that such a pattern is not realisable in small aspect ratio domains as it will also be shown in Section IV A.

The symmetries of the problem are: a) the mirror symmetry with respect to the axis $x = 1/2$

$$[u, w, T](x, z) \rightarrow [-u, w, T](1 - x, z), \quad (5)$$

which leaves the velocity and temperature field invariant, b) the mirror symmetry with respect to the axis $z = 1/2$

$$[u, w, T](x, z) \rightarrow [u, -w, 1 - T](x, 1 - z), \quad (6)$$

which leaves the velocity field invariant but transforms the temperature field into its opposite and c) the combination of these two symmetries, which is essentially a rotation by π with respect to the center of the cell $(x, z) = (1/2, 1/2)$. These symmetries dictate the bifurcations that the system can undergo.

III. NUMERICAL METHODS

A. Computation of multiple solutions with deflation

Steady-states solutions to Rayleigh–Bénard convection are computed using a recent numerical technique called deflation [20]. This algorithm is based on Newton’s method and allows the computation of multiple solutions to a nonlinear system of equations $F(\phi, \lambda) = 0$, where ϕ is the solution and $\lambda \in \mathbb{R}$ is a bifurcation parameter.

$$G(\phi, \lambda) := \left(\frac{1}{\|\phi - \phi_1\|^2} + 1 \right) F(\phi, \lambda), \quad (7)$$

such that $G(\phi, \lambda)$ does not converge to zero as $\phi \rightarrow \phi_1$. The term $\mathcal{M}(\phi, \phi_1) := \|\phi - \phi_1\|^{-2} + 1$ is called a deflation operator and ensures that Newton’s method applied again to G will not converge to a previously computed solution. By adding the unity in the expression of the deflation operator, we impose that the new problem G behaves similarly to F away from the root ϕ_1 . This process can be repeated to obtain a set of solutions $S(\lambda)$ to a nonlinear problem $F(\phi, \lambda) = 0$ at the bifurcation parameter λ . The next step is the continuation of the previously discovered solutions at a new bifurcation parameter $\lambda - \Delta\lambda$: each $\phi \in S(\lambda)$ is used as initial guess for the deflation procedure in order to construct a new set of solution $S(\lambda - \Delta\lambda)$ at $\lambda - \Delta\lambda$.

We apply this algorithm repeatedly to discover multiple solutions to the steady state Rayleigh–Bénard problem:

$$F(\phi, Ra) := \begin{cases} -\mathbf{u} \cdot \nabla \mathbf{u} - \nabla p + Pr \nabla^2 \mathbf{u} + Pr Ra T \hat{\mathbf{z}} & = 0, \\ \nabla \cdot \mathbf{u} & = 0, \\ -\mathbf{u} \cdot \nabla T + \nabla^2 T & = 0, \end{cases} \quad (8)$$

where $\phi = (\mathbf{u}, p, T)$ and Ra is the bifurcation parameter. This equation is discretised with Taylor–Hood finite elements for the velocity and pressure (piecewise biquadratic and piecewise bilinear respectively), together with piecewise bilinear polynomials for the temperature, using the Firedrake finite element library [38]. The unit square domain is represented by a mesh with 50×50 square cells to preserve the symmetries of the problem and avoid numerical artefacts. A coarse discretization is needed due to the complexity of the problem and number of distinct solutions discovered, leading to hundred of thousands of deflation steps and Newton iterations. Moreover, we have not observed significant differences in selected experiments where we refined the mesh. A crucial question in the deflation technique is the choice of the deflation operator \mathcal{M} because it can affect the convergence of Newton’s method. We use the following operator,

$$\mathcal{M}((\mathbf{u}, p, T), (\mathbf{u}_1, p_1, T_1)) = \left(\frac{1}{\|\mathbf{u} - \mathbf{u}_1\|_2^2 + \|\nabla(\mathbf{u} - \mathbf{u}_1)\|_2^2 + \|T - T_1\|_2^2} + 1 \right), \quad (9)$$

where $\|\cdot\|_2$ denotes the L^2 -norm. It is important to note that the deflation operator \mathcal{M} does not depend on the pressure p because we wish to deflate all the solutions of the form $(\mathbf{u}_1, p_1 + c, T_1)$, where $c \in \mathbb{R}$, to avoid discovering solutions trivially related to known ones.

We perform bifurcation analysis of Rayleigh–Bénard convection and compute solutions to the nonlinear system of Eq. (8) for $0 \leq Ra \leq 10^5$ using deflated continuation [20, 21]. This method combines deflation with continuation of the solutions in the bifurcation parameter in order to continue and discover new branches of solutions as we decrease the bifurcation parameter from $Ra = 10^5, 10^5 - \Delta Ra, \dots, 0$. Here, ΔRa denotes the continuation step size in the bifurcation parameter, which is chosen to be equal to $\Delta Ra = 100$. In a previous work on the computation of solutions to the 3D nonlinear Schrödinger equation [26], we found that having good initial guesses (e.g. solutions of the linearised problem) for the initial deflation steps facilitates the convergence of Newton’s method and leads to more complex and interesting states. However, contrary to [26] we do not have the analytical expressions of the linear solutions to the Rayleigh–Bénard convection due to the no-slip boundary conditions. Therefore, we numerically solve an eigenvalue problem (see Section III B) to obtain the first ten unstable eigenmodes $(\mathbf{u}_1, T_1), \dots, (\mathbf{u}_{10}, T_{10})$ linearised around the conducting steady state Eq. (4) (see Fig. 2). Then, the sums of the conducting state with the respective normalized perturbations: $(\mathbf{u}_1, 1 - z + T_1), \dots, (\mathbf{u}_{10}, 1 - z + T_{10})$ are used as initial guesses for deflated continuation.

B. Linear stability analysis

The stability analysis of a given steady state (\mathbf{u}_0, T_0) is performed by considering the perturbation ansatz

$$\mathbf{u}(x, z, t) = \mathbf{u}_0 + \mathbf{v} e^{\lambda t}, \quad (10a)$$

$$T(x, z, t) = T_0 + \theta e^{\lambda t}, \quad (10b)$$

where the velocity perturbation $\mathbf{v} \ll 1$ and the temperature perturbation $\theta \ll 1$ have an eigenvalue or growth rate λ . When at least one of the eigenvalues has a positive real part $\mathcal{R}(\lambda) > 0$, we can have two types of instabilities. The stationary instability which occurs when the imaginary part of the eigenvalue $\mathcal{I}(\lambda) = 0$ and the oscillatory instability which occurs when $\mathcal{I}(\lambda) \neq 0$. If all the eigenvalues have negative real parts, then the perturbed steady state is stable. Inserting Eq. (10) into Eq. (1) and considering the linearised system of equations, we obtain the following generalised eigenvalue problem at leading order

$$\begin{pmatrix} A & -\nabla & RaP_r\hat{\mathbf{z}} \\ \nabla \cdot & 0 & 0 \\ -\nabla T_0 \cdot & 0 & \nabla^2 - \mathbf{u}_0 \cdot \nabla \end{pmatrix} \begin{pmatrix} \mathbf{v} \\ p \\ \theta \end{pmatrix} = \lambda \begin{pmatrix} I & 0 & 0 \\ 0 & 0 & 0 \\ 0 & 0 & I \end{pmatrix} \begin{pmatrix} \mathbf{v} \\ p \\ \theta \end{pmatrix}, \quad (11)$$

where I is the relevant identity operator and A is the linear operator defined by

$$A\mathbf{v} = \nabla^2\mathbf{v} - \mathbf{u}_0 \cdot \nabla \mathbf{v} - \mathbf{v} \cdot \nabla \mathbf{u}_0.$$

The eigenvalue problem described in Eq. (11) is solved with a Krylov–Schur method [39] using the SLEPc library [40].

To obtain the critical value of the Rayleigh number Ra_c at which the conducting state Eq. (4) becomes unstable, we modify the eigenvalue problem in Eq. (11). Inserting Eq. (4) into Eq. (11) we obtain the following generalized eigenvalue problem

$$\begin{pmatrix} \nabla^2 & -\nabla & RaP_r\hat{\mathbf{z}} \\ \nabla \cdot & 0 & 0 \\ \hat{\mathbf{z}} \cdot & 0 & \nabla^2 \end{pmatrix} \begin{pmatrix} \mathbf{v} \\ p \\ \theta \end{pmatrix} = \lambda \begin{pmatrix} I & 0 & 0 \\ 0 & 0 & 0 \\ 0 & 0 & I \end{pmatrix} \begin{pmatrix} \mathbf{v} \\ p \\ \theta \end{pmatrix}. \quad (12)$$

A steady state becomes unstable when $\lambda = 0$ and this corresponds to the critical Rayleigh number Ra_c which is the smallest Ra satisfying Eq. (12) for $\lambda = 0$. So, to obtain the critical value of the Rayleigh number for different base states we have reformulated the problem to a generalised eigenvalue problem for Ra_c as follows

$$\begin{pmatrix} \nabla^2 & -\nabla & 0 \\ \nabla \cdot & 0 & 0 \\ \hat{\mathbf{z}} \cdot & 0 & \nabla^2 \end{pmatrix} \begin{pmatrix} \mathbf{v} \\ p \\ \theta \end{pmatrix} = Ra_c \begin{pmatrix} 0 & 0 & -P_r\hat{\mathbf{z}} \\ 0 & 0 & 0 \\ 0 & 0 & 0 \end{pmatrix} \begin{pmatrix} \mathbf{v} \\ p \\ \theta \end{pmatrix}. \quad (13)$$

In the following sections this linear analysis will be used to study the stability of the conducting state Eq. (4) and of the nonlinear steady state solutions that we obtain from deflated continuation.

IV. RESULTS

A. Primary instabilities

In this section, we analyse the stability of the conducting steady state defined by Eq. (4). We found that the first instability of this state arises at $Ra_c^{(1)} := Ra_c \approx 2586$. However, it is well known [41] that the critical Rayleigh number is approximatively equal to $Ra_c^* \approx 1707.762$ for an unbounded domain with periodic streamwise boundaries and no-slip spanwise boundaries. This difference in the value of Ra_c is due to the effect of the side walls on the instability. This effect should decrease when x becomes large such that the behaviour predicted for an unbounded domain is recovered. To demonstrate this, we systematically increase the aspect ratio

$$\Gamma = \frac{L}{d}, \quad (14)$$

by fixing the height $d = 1$ and increasing the length L of the domain. Figure 1 (left) clearly shows that for $\Gamma \gg 1$ the $Ra_c^{(1)}$ converges to Ra_c^* . Note, however, that this is not the case for the spatially extended system with stress-free boundary conditions in the limit of $\Gamma \gg 1$ due to the presence of hidden symmetries [42]. Therefore, only the large aspect ratio system in the case of no-slip boundary conditions can be considered as a small perturbation of the unbounded system. In addition, we systematically decrease Γ by fixing d and decreasing the length L of the domain. For aspect ratios $\Gamma < 1$ we observe $Ra_c \propto \Gamma^{-3.88}$ indicating a more stable flow as Γ decreases. The critical Rayleigh number for Rayleigh–Bénard convection with stress-free boundary conditions is $Ra_c^*(k) = (\pi^2 + k^2)^3/k^2$ [43], where k is the horizontal wavenumber. For $k \gg 1$ the critical Rayleigh number scales like $Ra_c^*(k) \propto k^4 \propto L^{-4} \propto \Gamma^{-4}$ using Eq. (14). This scaling relation is very close to the observed one, which implies that the exponent is not affected much by the no-slip boundary conditions. The exponent we find is in agreement with [44].

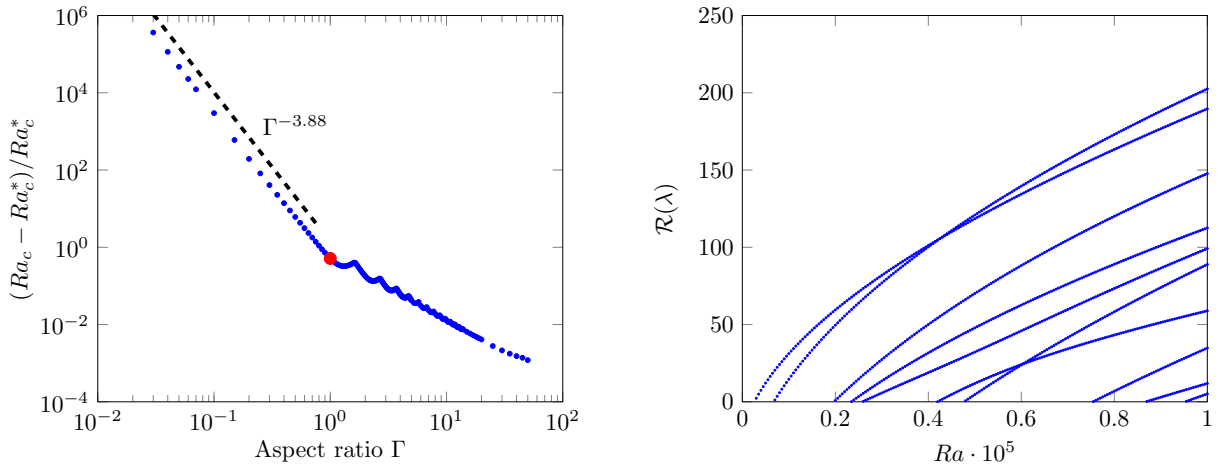


FIG. 1. (Color online) Left: Critical Rayleigh number with respect to the aspect ratio Γ (blue dots). The red dot indicates the aspect ratio $\Gamma = 1$, which is the focus of our study. Right: Real part of the growth rate of the eigenmodes that emanate from the conducting steady state.

TABLE I. The ten primary bifurcations from the conductive state within the range $0 \leq Ra \leq 10^5$. Here n enumerates the eigenmodes by order of appearance as Ra increases.

n	1	2	3	4	5	6	7	8	9	10
$Ra_c^{(n)}$	2586	6746	19655	23346	25780	41772	47431	74878	86313	94543
(k_x, k_z)	(2,1)	(3,1)	(4,1)	(3,2)	(2,2)	(4,2)	(5,1)	(5,2)	(3,3)	(4,3)

The case on which we focus for the rest of the paper is the square cell ($\Gamma = 1$), which is denoted with a red dot in Fig. 1 (left). We first study the linear stability of the conducting state Eq. (4). In the range $0 \leq Ra \leq 10^5$ we observe 10 supercritical stationary bifurcations that arise from the conducting state. Figure 1 (right) shows the real part of the growth rate of the unstable eigenmodes as a function of Ra . The onset of these bifurcations occur when $\mathcal{R}(\lambda) = 0$. The critical values of the Rayleigh number at the onsets are listed in Table I. Figure 1 (right) demonstrates that the growth rates of the eigenmodes vary with Rayleigh number and they have different dependence. The eigenmode which bifurcated from the conducting state at $Ra_c^{(2)} = 6746$ ends up being the most unstable as $Ra \rightarrow 10^5$.

The velocity magnitude and temperature fields of the eigenmodes from these primary bifurcations of the flow are shown in Fig. 2 with the corresponding critical Rayleigh numbers indicated on the top of each flow pattern. In Table I we characterise the flow patterns by their Fourier modes (k_x, k_z) , where k_x is the streamwise wavenumber and k_z is the spanwise wavenumber of the Fourier modes of the temperature field. Note that due to the small aspect ratio of the domain the flow pattern of the first bifurcation at $Ra_c^{(1)} = 2586$ is just a single convection roll (see Fig. 2) instead of two counter-rotating rolls as it is known from the classical result. In the following sections, we first analyse the branches of solutions that are created from some of these primary bifurcations before moving to disconnected branches.

B. Bifurcation diagrams

The combination of deflated continuation and the initialisation strategy presented in Section III A identified 129 solutions to the two-dimensional steady-state Rayleigh–Bénard convection at $Ra = 10^5$ including 43 unique solutions with respect to the symmetries. Here, we analyse the evolution and the linear stability of some of the branches arising from the first four excited states (see Fig. 2) as well as two disconnected branches. Moreover, we discard the mirror symmetric solutions with respect to the $x = 1/2$ and $z = 1/2$ axis (see symmetries in Section II).

Our diagnostics for the bifurcation diagrams, representing the evolution of the steady states as a function of Ra ,

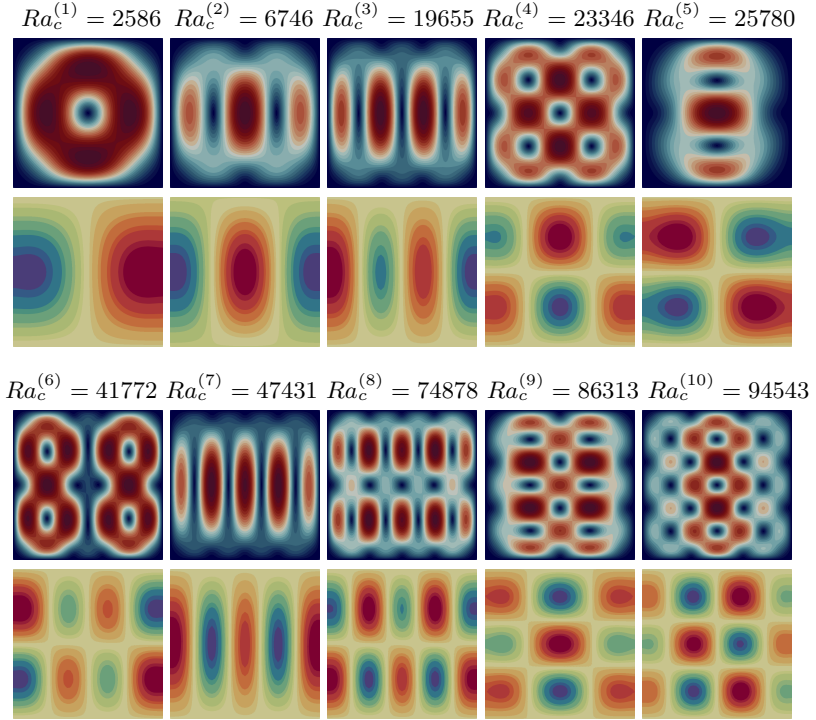


FIG. 2. (Color online) The eigenmodes of the primary bifurcations emanating from the conducting steady state solution Eq. (4) in the Rayleigh number range $0 \leq Ra \leq 10^5$. The top rows show the magnitude of the velocity \mathbf{v} (red color indicates a high magnitude and blue a zero velocity profile), while the bottom rows show the temperature θ (red and blue respectively display positive and negative temperature fields).

are the kinetic energy $\|\mathbf{u}\|_2^2$, the potential energy $\|T\|_2^2$, and the Nusselt number Nu , which are defined as

$$\|\mathbf{u}\|_2^2 = \int \mathbf{u}^2 d^2x, \quad \|T\|_2^2 = \int T^2 d^2x, \quad Nu = \int |\nabla T|^2 d^2x. \quad (15)$$

The Nusselt number characterises the efficiency of convective heat transfer and is given by the ratio of the total heat transfer (i.e. both advective and diffusive) to the conductive heat transfer $Nu \equiv HL/\kappa d = \langle wT \rangle - \kappa \partial_z \langle T \rangle = \langle (\nabla T)^2 \rangle$, where H is the heat flux and $\langle \cdot \rangle$ stands for the area average. A Nusselt number of one represents heat transfer by pure conduction. Here, the Nusselt number is essentially defined as the dissipation rate of the temperature variance (see second equality). This is obtained by integrating the equation for potential energy over the entire area [45].

The bifurcation diagrams are presented in Fig. 3, where the numbers denote the different branches of steady solutions, highlighting the values of kinetic energy, potential energy and Nusselt number that correspond to each branch on each diagram.

The first steady state solutions that we obtain from deflated continuation as Ra is varied are four branches that arise from the first four bifurcations of the conducting steady state: branch (1) at $Ra_c^{(1)} = 2586$, branch (2) at $Ra_c^{(2)} = 6746$, branch (3) at $Ra_c^{(3)} = 19655$ and branch (4) at $Ra_c^{(4)} = 23346$. Moreover a secondary branch (5) bifurcates at $Ra \approx 13550$ from branch (2), which originates from the second instability of the conducting state. A similar behaviour is observed for the fourth instability, where branch (6) bifurcates at $Ra \approx 27300$ from branch (4). We also focus on two disconnected branches (7) and (8) obtained directly by deflated continuation. In the bifurcation diagram of kinetic energy (see Fig. 3(a)), branch (7) is close to branch (3). However, note that branch (7) does not bifurcate from branch (3) according to the bifurcation diagram of the potential energy (see Fig. 3(b)). On the other hand, branch (8) bifurcates from branch (7) at $Ra \approx 37000$ (see Fig. 3).

It is interesting to point out that in the range $0 \leq Ra \leq 10^5$ branch (1) has the highest kinetic energy while branch (6) has the highest potential energy (see Fig. 3(a) and 3(b)). The steady state solutions that are most effective in convecting heat transfer for $0 \leq Ra \lesssim 3 \times 10^4$ are in branch (1) from the first instability of the conducting state while for $3 \times 10^4 \lesssim Ra \leq 9.5 \times 10^4$ are in the branch (2), and in branch (7) for $Ra \gtrsim 9.5 \times 10^4$ (see Fig. 3(c)).

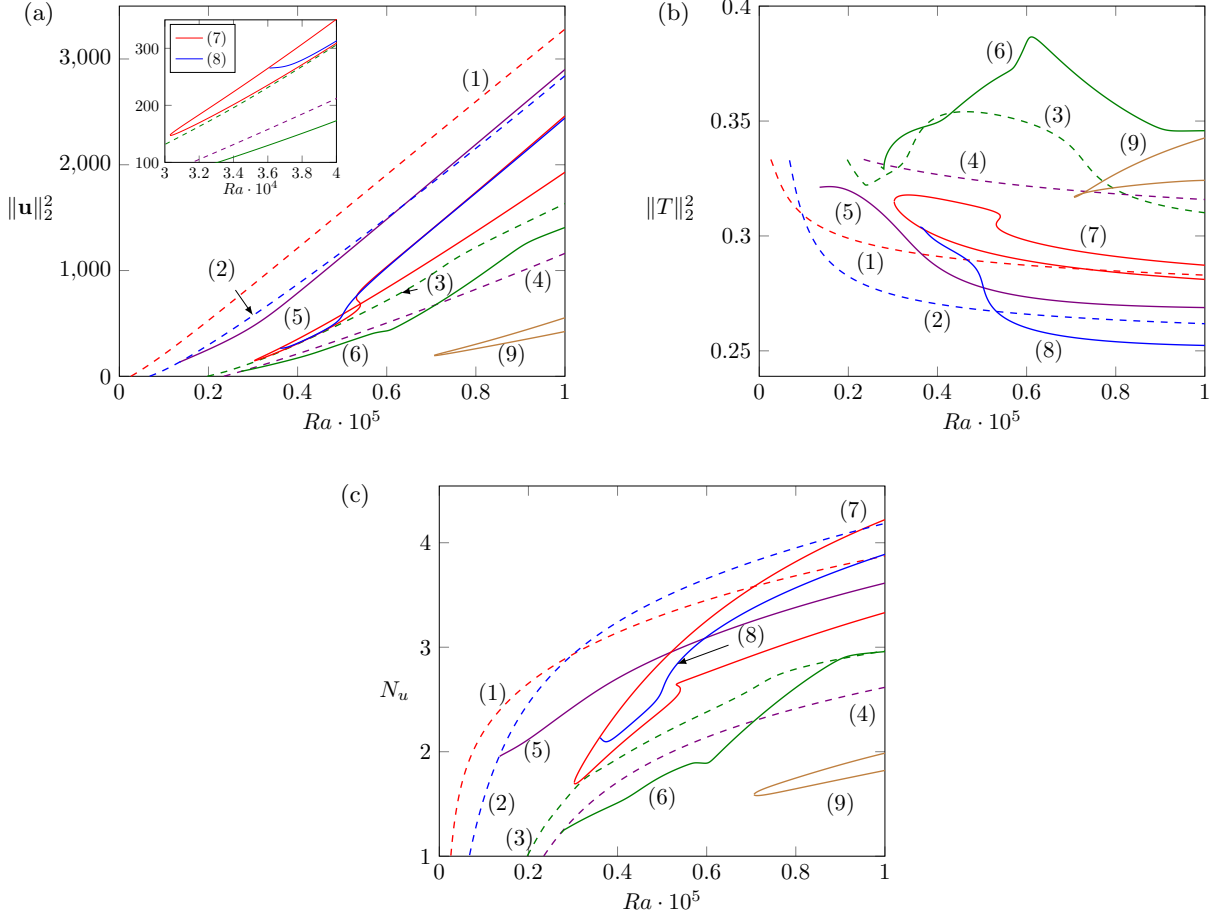


FIG. 3. (Color online) Bifurcation diagram of the kinetic energy $\|\mathbf{u}\|_2^2$ of the branches discovered by deflation (a). The panels (b)-(d) represent the bifurcation diagrams of the kinetic energy, the potential energy $\|T\|_2^2$, and the Nusselt number Nu , respectively, for the branches studied in this paper. The branches that originate from the linear instabilities are highlighted in dashed lines while bifurcations and disconnected branches are depicted with solid lines.

C. Bifurcations from the conducting steady state

In this section we analyse the states that emanate from the conducting steady state and their evolution as a function of the bifurcation parameter Ra . Our analysis involves the detailed evolution of the velocity magnitude and the temperature fields on the branches of the bifurcation diagrams of kinetic and potential energy, respectively. In addition, we present the real and imaginary parts of the largest growth rates from the linear stability analysis we have performed on the steady state solutions.

Figure 4 shows results of the aforementioned analysis for branch (1), which arises at $Ra_c^{(1)} = 2586$ from the first eigenmode (see Fig. 2). This bifurcation breaks only the rotational symmetry by π that is satisfied by the eigenmode. As Ra increases, the magnitude of the velocity field evolves from a circular to a bent convection roll at $Ra \approx 4 \times 10^4$ (see Fig. 4(a)). On the other hand, the z-shaped interface of the temperature field is sheared (see Fig. 4(b)), enhancing the heat transfer in the convection cell (see also branch (1) in Fig. 3(c)). Figure 4(c) demonstrates that the steady state solution of this branch remains stable ($\mathcal{R}(\lambda) < 0$) under perturbations with a constant growth rate over the whole range of Rayleigh numbers we consider. The imaginary part of the largest growth rate is zero from the stationary bifurcation at $Ra_c^{(1)} = 2586$ to the $Ra = 10^5$ (see Fig. 4(d)), while the subsequent growth rate has a strong oscillatory component and its real part is $\mathcal{R}(\lambda) = \text{const} < 0$.

The second eigenmode introduced in Fig. 2 gives birth to branch (2) at $Ra_c^{(2)} = 6746$, which is depicted in Fig. 5(a)-(b). While the symmetry of the eigenmode with respect to the x -axis is rapidly broken, the velocity and temperature profiles remain symmetric with respect to the z -axis in the range of parameters that we consider. Then, the largest growth rate in Fig. 5(c) indicates that the perturbed steady state solutions of this branch is stable over the interval $Ra \in [13500, 85500]$ and exponentially unstable outside. A bifurcation occurs at $Ra \approx 13500$ when $\mathcal{R}(\lambda) = 0$, which

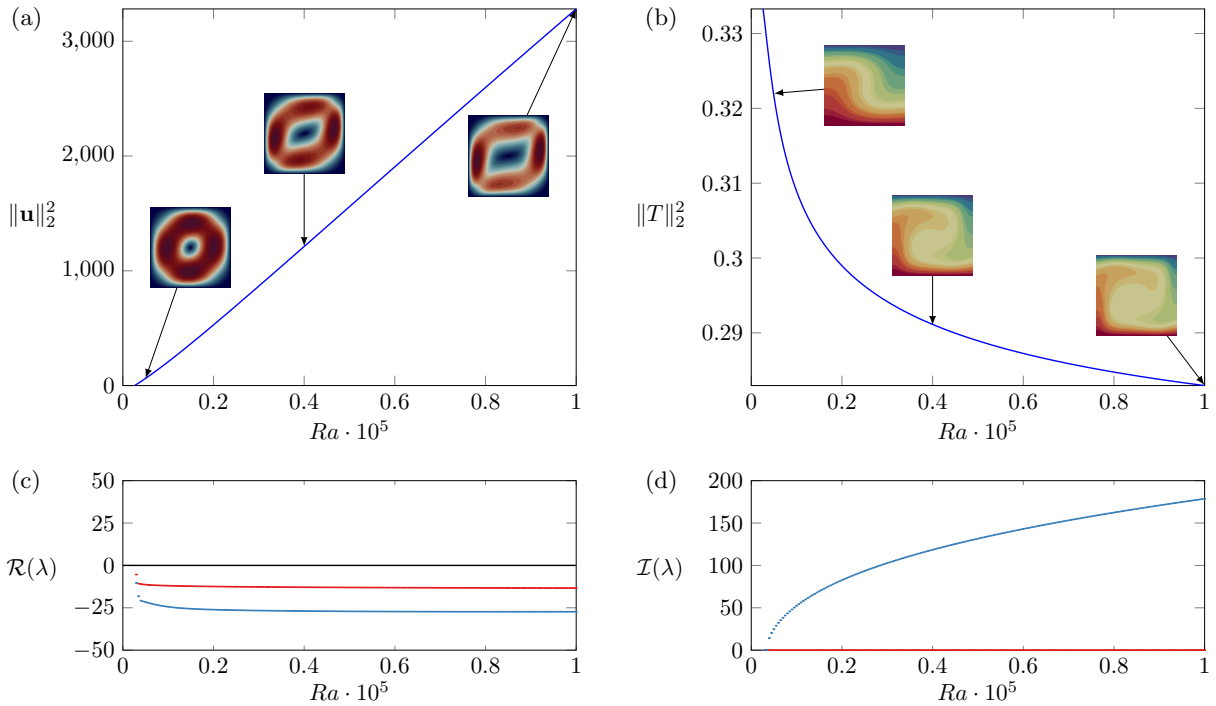


FIG. 4. (Color online) Evolution of the steady state flow patterns for (a) the kinetic energy and (b) the potential energy of branch (1), which arises from the first eigenmode. The color scheme for the temperature field ranges from 0 (blue) to 1 (red). The real and positive imaginary parts of the largest growth rates are presented in (c) and (b), respectively.

is analysed later and represented in Fig. 6. Another bifurcation is observed at $Ra \approx 85500$ and has been obtained by deflated continuation.

Figure 6(a) demonstrates that the three symmetries of the second eigenmode (see Section II) are rapidly broken in the bifurcating branch (5) as Ra increases. This symmetry breaking leads to a primary large scale circulation spanning the domain and a secondary vortex with smaller amplitude in one of the corners depending on which symmetric solution one is referring to. As $Ra \rightarrow 10^5$, the difference in the flow pattern of the velocity magnitude between branch (1) and (5) is the secondary vortex in the corner of the convection cell. The symmetry breaking is also obvious in the temperature field (see Fig. 6(b)) with the potential energy of the flow to decrease slightly in contrast to the increase of the kinetic energy and the convective heat transfer (see also Fig. 3(c)). The largest growth rate shows that the states are unstable to perturbations without any oscillations (see Fig. 6(d)). The subsequent growth rates shown in Fig. 6(c) are negative and almost constant in this range of Rayleigh numbers.

Branch (3) originates from the eigenmode of the conducting state at $Ra_c^{(3)} = 19655$, which is depicted in Fig. 7. Similarly to branch (5), the three symmetries (see Section II) satisfied by the third eigenmode are rapidly broken and the pattern of the velocity magnitude becomes more complex as Ra increases. This complex pattern is one reason for the meandering of the potential energy in this range of Rayleigh numbers and enhances the convective heat transfer (see Fig. 3(c)) by mixing the temperature field. Figure 7(c) shows that the steady-state solutions of branch (3) are stationary unstable under the effect of perturbations until $Ra \approx 39500$. At this Rayleigh number, we see that the two most unstable eigenmodes coalesce into an unstable eigenmode with an oscillating growth rate (see Fig. 7(d)). All the subsequent eigenmodes are found to be stable with either $\mathcal{I}(\lambda) = 0$ or $\mathcal{I}(\lambda) \neq 0$.

Figure 8 shows bifurcation diagrams and the linear stability results of branch (4) which was originated from the fourth linear eigenmode at $Ra_c^{(4)} = 23346$. The flow pattern of the velocity magnitude has a symmetric form of an array of four vortices, which is almost conserved over the whole range of the Rayleigh numbers we consider as Fig. 8(a) illustrates. Similarly, the symmetric pattern of the temperature field remains almost unaffected in the regime $23346 \leq Ra \leq 10^5$ (see Fig. 8(b)). Actually, the bifurcation breaks symmetry (6) and the rotational symmetry by π of the eigenmode. This is visible within this range of Ra by inspecting the flow patterns displayed on the diagram of potential energy.

Figure 8(c) shows the real parts of the four largest growth rates as a function of Ra . At Rayleigh numbers close to $Ra_c^{(4)} = 23346$ we see that the three eigenmodes are stationary unstable, while the fourth one is stationary stable. As Ra increases the first with the third most unstable eigenmode (coloured in red and green, respectively, in Fig. 8(c))

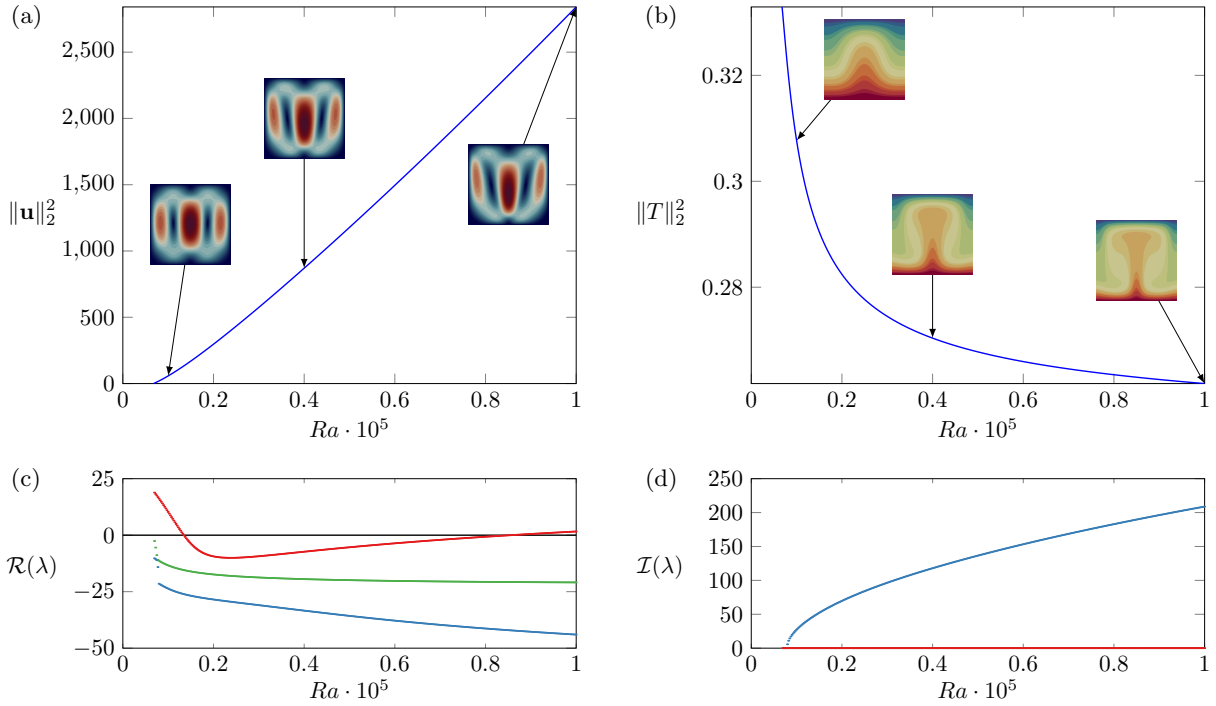


FIG. 5. (Color online) Evolution of the steady state flow patterns for (a) the kinetic energy and (b) the potential energy of branch (2), which arises from the second eigenmode. The real and positive imaginary parts of the largest growth rates are presented in (c) and (b), respectively. The two largest growth rates are shown in red and green while the subsequent ones are depicted in blue.

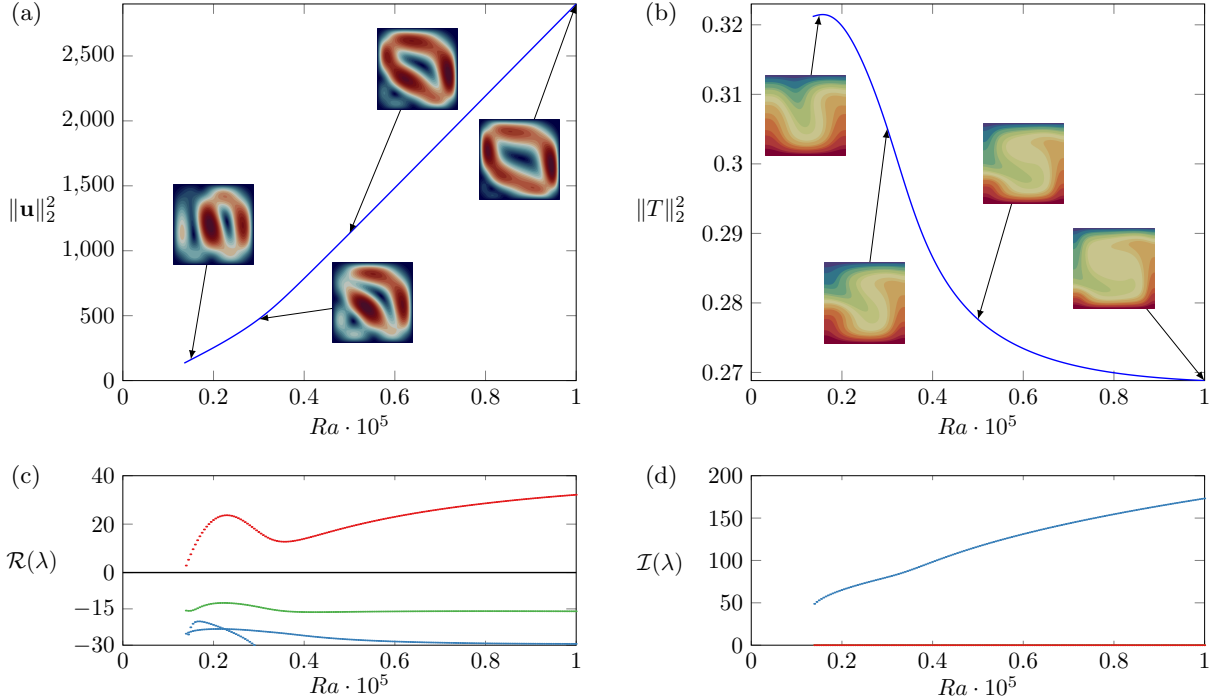


FIG. 6. (Color online) Evolution of the steady state flow patterns for (a) the kinetic energy and (b) the potential energy of branch (5), which bifurcates from branch (2) at $Ra \approx 13550$. The real and positive imaginary parts of the largest growth rates are presented in (c) and (b), respectively.

coalesce at $Ra \approx 56000$ into an oscillatory unstable eigenmode whose growth rate and oscillation frequency increases

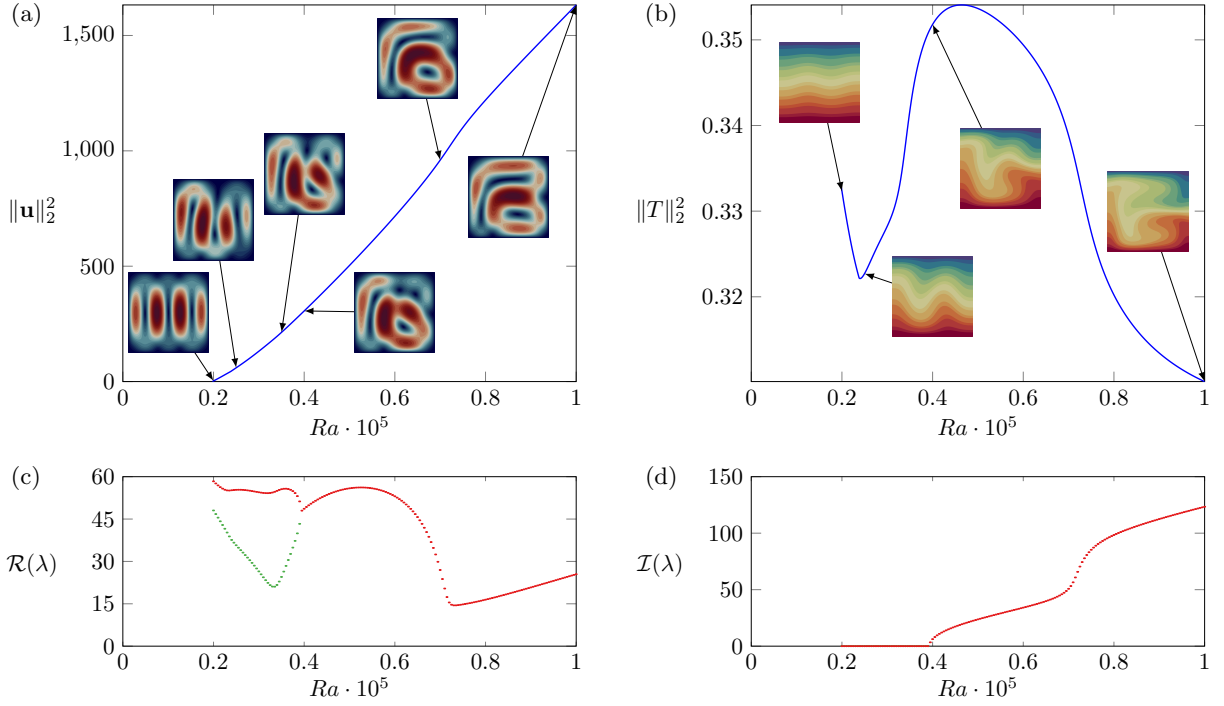


FIG. 7. (Color online) Evolution of the steady state flow patterns for (a) the kinetic energy and (b) the potential energy of branch (3), which arises from the third eigenmode. The real and positive imaginary parts of the largest growth rates are presented in (c) and (b), respectively.

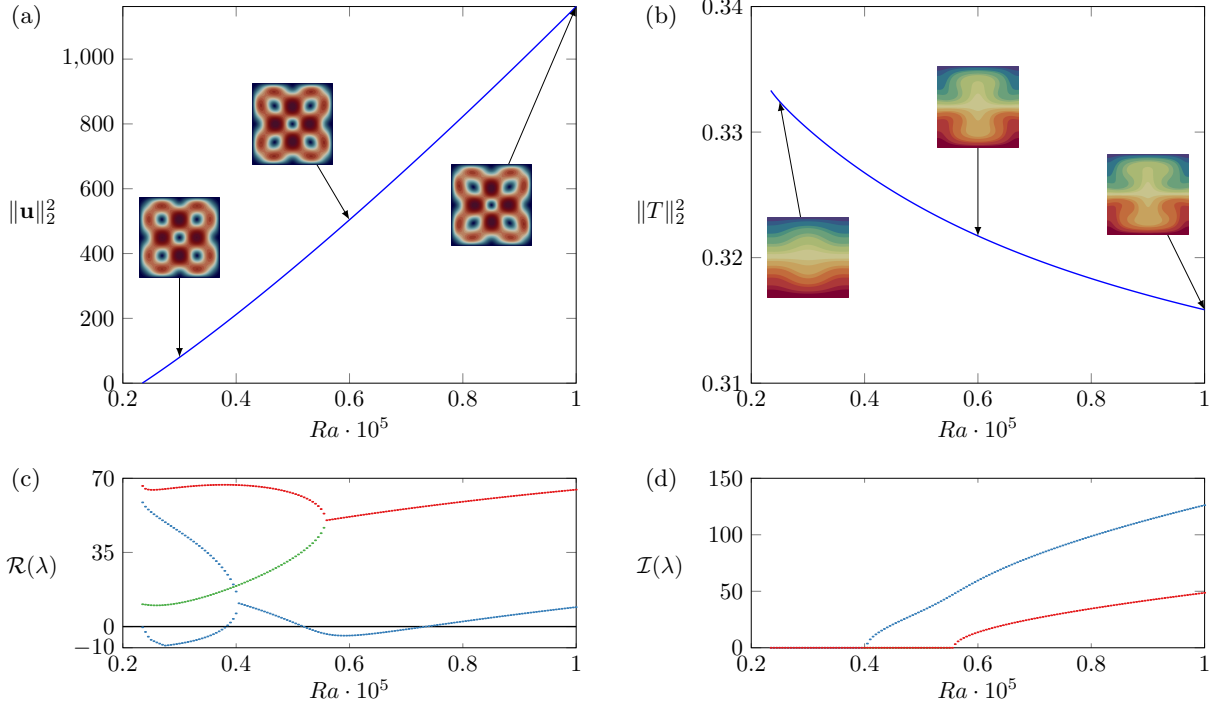


FIG. 8. (Color online) Evolution of the steady state flow patterns for (a) the kinetic energy and (b) the potential energy of branch (4), which arises from the fourth eigenmode. The real and positive imaginary parts of the largest growth rates are presented in (c) and (b), respectively.

as $Ra \rightarrow 10^5$. Similarly, the second and fourth most unstable mode coalesce at $Ra \approx 40000$ to create an eigenmode

which is oscillatory unstable for $40000 < Ra \leq 10^5$.

We close our discussion on the branches arising from the conducting steady state solution with branch (6), presented in Fig. 9. This branch bifurcates from branch (4) at $Ra \approx 27300$. This bifurcation breaks first the rotational symmetry

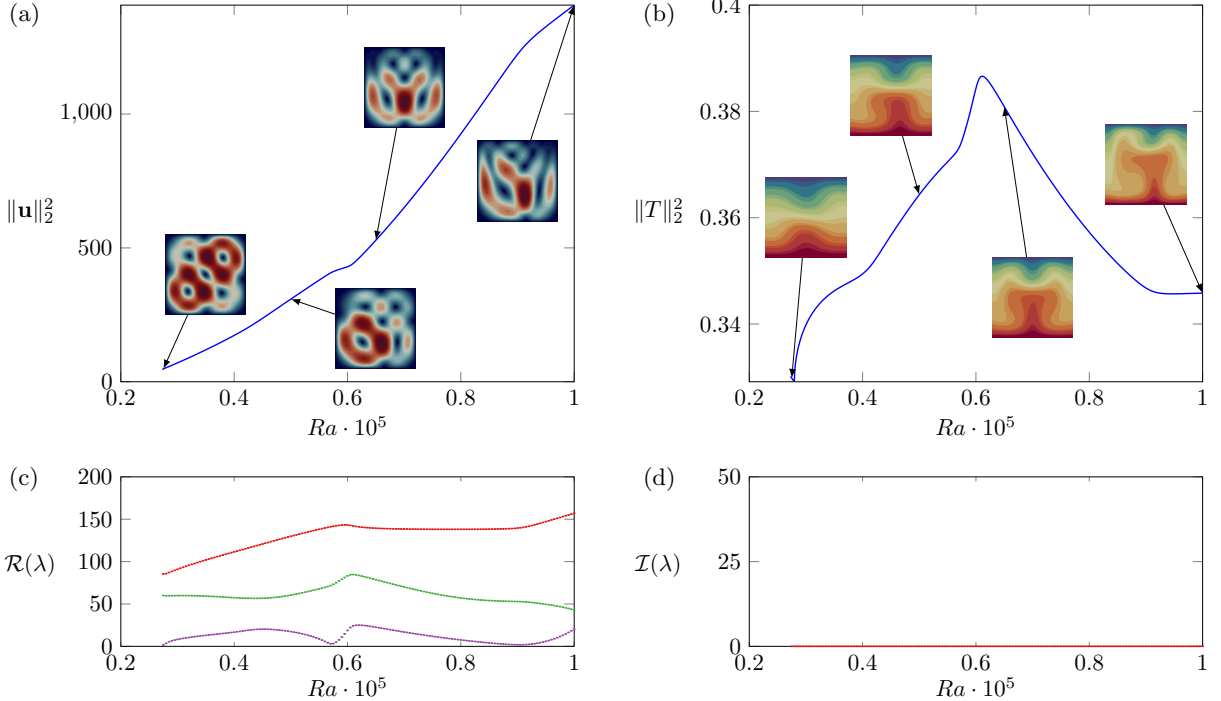


FIG. 9. (Color online) Evolution of the steady state flow patterns for (a) the kinetic energy and (b) the potential energy of branch (6), which bifurcates from branch (4) at $Ra \approx 27300$. The real and positive imaginary parts of the largest growth rates are presented in (c) and (b), respectively.

by π of the flow pattern with the four vortices. Close to $Ra \approx 50000$ we see that all the three basic symmetries (see Section II) are broken and it is of interest that at $Ra \approx 60000$ symmetry (5) is restored in the flow which breaks again to a non-symmetric flow pattern as $Ra \rightarrow 10^5$. The linear stability analysis of this branch shows that the steady states are very sensitive to perturbations and thus stationary unstable throughout the range of Ra considered in this study.

D. Disconnected branches

We now focus on the disconnected branch (7) (see Fig. 3), which comprises an upper and a lower branch, depicted in blue and red in Fig. 10, respectively. At the upper (blue) branch the flow pattern of the velocity magnitude is a three vortex state with one large tilted vortex spanning the domain and two smaller vortices located at the corners. As $Ra \rightarrow 10^5$ we notice that the state looks similar to the branches (1) and (5). The difference is that branch (5) involves only one smaller vortex at the corner of the domain and branch (1) has no vortices at the corners, while branch (7) has two smaller vortices located at the corners. At $Ra \approx 52000$ the branch takes the form of an s-shape bifurcation with hysteresis, similar to the cusp bifurcation [46]. As the s-shape bifurcation is approached from below the real part of the growth rate of the most unstable eigenmode decreases toward zero at the critical point (see Fig. 10(c)). Above the s-shape bifurcation $\mathcal{R}(\lambda)$ increases and seems to saturate as $Ra \rightarrow 10^5$. The imaginary part of the growth rate is zero in the whole range of Ra numbers suggesting that the perturbed steady state is stationary unstable in this regime. The potential energy of the upper (blue) branch decreases with Ra in contrast to the kinetic energy. As Ra increases the flow pattern of the potential energy becomes more efficient at transferring heat due to the large scale circulation in the flow (see Fig. 3(c)).

The upper (blue) branch plays an important role on the nonlinear dynamics of Rayleigh-Bénard convection at values of $Ra > 10^5$. The flow pattern of the kinetic energy shown for $Ra = 10^5$ (see Fig. 10(a)), with the large scale vortex and the two smaller vortices at the corners of the domain, is reminiscent to the flow patterns from studies on the dynamics of random-in-time flow reversals [29–31, 47]. These reversals in the flow direction of the large scale

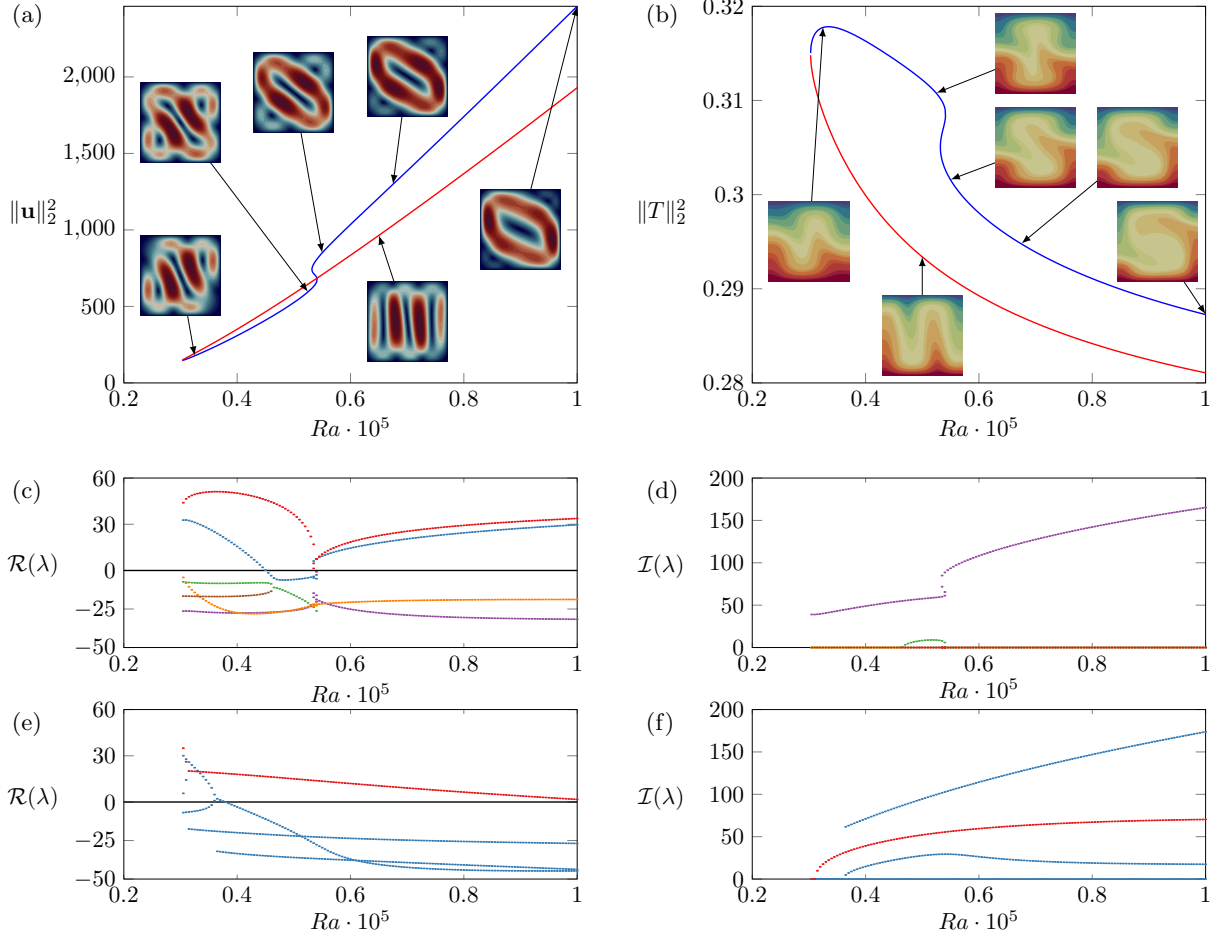


FIG. 10. (Color online) Evolution of the steady state flow patterns for (a) the kinetic energy and (b) the potential energy of the disconnected branch (7). The upper and lower parts of the branch are coloured in blue and red, respectively. The real and positive imaginary parts of the largest growth rates of the upper (resp. lower) part of the branch are presented in (c) and (b) (resp. (e) and (f)), respectively.

circulation at irregular time intervals have been observed in domains with free-slip or no-slip boundaries and in a narrow band of Rayleigh numbers in the range $10^7 \leq Ra \leq 10^9$ depending on the Prandtl number [29–31]. In this regime the system fluctuates in time between essentially the state we show for $Ra = 10^5$ (see Fig. 10(a)) and its mirror symmetric state. Therefore, for values of the bifurcation parameter $Ra > 10^5$ we expect the perturbed steady states of this branch to gradually become stable as they turn out to be the statistically steady state solution in the range $10^7 \leq Ra \leq 10^9$. So, as Ra increases from 10^5 to 10^9 the system transitions from one steady state solution to another. This big change in the dynamics of the flow are caused by bifurcations over a turbulent background [27]. Such bifurcations have been observed in many other types of flows [48–52] and understanding their dynamics is an open question of great interest.

At the lower (red) branch illustrated in Fig. 10(a) we observe the central vortex to be oriented more vertically, giving space to the smaller vortices at the corners to extend along the z axis and almost reach the height of the domain. This flow pattern is an extension of the two-vortex pattern observed in branch (5) (see Fig. 6) and it has similar features to the three-vortex pattern found near the linear limit of branch (3) (see Fig. 7). The patterns of the kinetic and potential energy of this branch are almost invariant within the range $30000 \lesssim Ra \leq 10^5$. The flow pattern of the potential energy clearly manages to effectively push the hot fluid toward the cold plate at the top and vice versa. This efficiency in convective heat transfer is clearly depicted in Fig. 3(c), where this part of branch (7) has the highest Nusselt number for $Ra > 95000$.

Analysing the stability of the lower (red) branch, we find that the perturbed steady states solutions become increasingly more stable as the Rayleigh number increases with $R(\lambda) \approx 0$ at $Ra = 10^5$ (see Fig. 10(e)). On the other hand, the imaginary part of the growth rate $I(\lambda) = 0$ at the threshold of the disconnected branch and as Ra increases the instability becomes progressively oscillatory (see Fig. 10(f)). The subsequent growth rates presented in Fig. 10(e)

remain negative as Ra increases suggesting that this part of branch (7) is another preferred steady state solution of the system particularly for $Ra > 10^5$.

Branch (8) illustrated in Fig. 11 bifurcates from the lower part of the disconnected branch (7) at $Ra \approx 37000$ (see also Fig. 3). In this case, the pattern of the kinetic energy transitions into a main bent vortex with a vertically

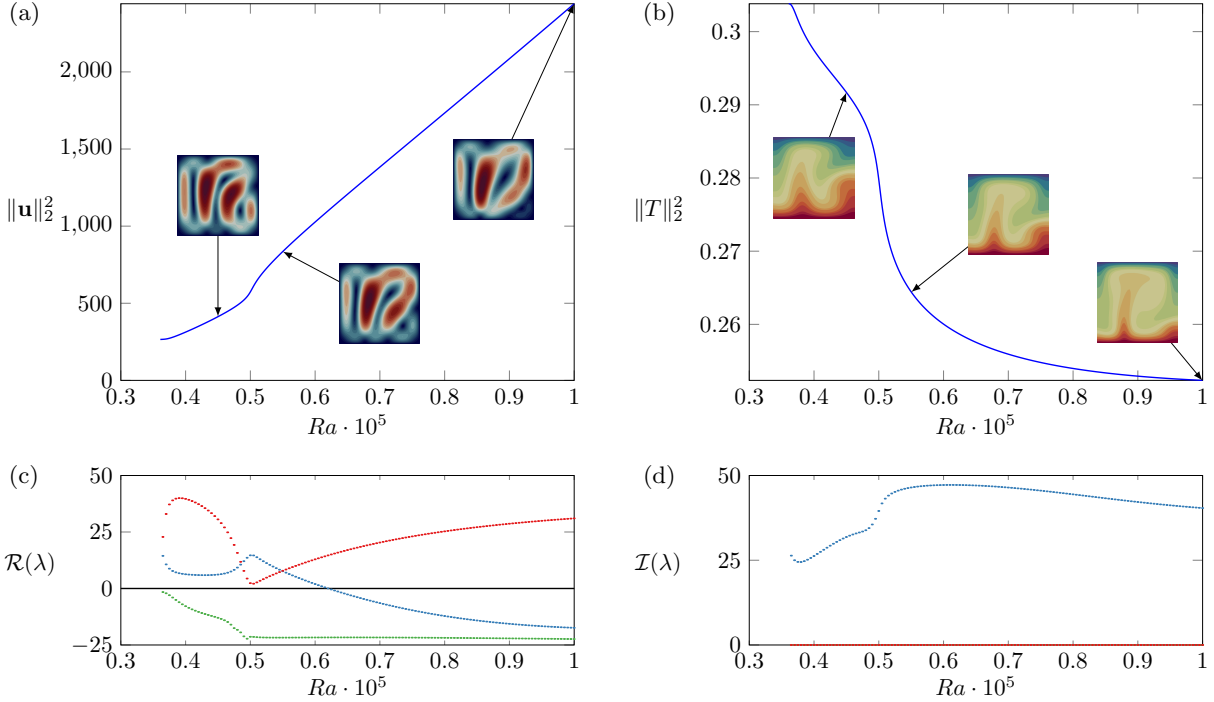


FIG. 11. (Color online) Evolution of the steady state flow patterns for (a) the kinetic energy and (b) the potential energy of branch (8), which bifurcates from the lower part of the disconnected branch (7) at $Ra \approx 37000$. The real and positive imaginary parts of the largest growth rates are presented in (c) and (b), respectively.

elongated vortex on its left and a smaller vortex at the bottom right corner (see Fig. 11(a)). From Fig. 3 we can see that even though the kinetic energy of branch (8) is equal to that of the upper part of branch (7) for $Ra > 50000$, the potential energy is much smaller and apparently the smallest among the branches we have considered. The pattern of the potential energy is essentially a hot plume that rises effectively all the way to the cold plate (see Fig. 11(b)). This flow pattern becomes increasingly more efficient at transferring heat across the domain as Ra increases (see Fig. 3(c)). However, it is not as efficient in convecting heat as the pattern of branch (7) (see lower branch in 10(b)) because two hot plumes are obviously more effective than one. The steady state solution of branch (8) is stationary unstable to finite perturbations over the range $37000 \lesssim Ra \leq 10^5$ except for a small range around $Ra = 50000$ where it becomes oscillatory unstable. This can be seen from Fig. 10(c) and 10(d), where the two largest growth rates (coloured in red and blue) swap with each other in this small range of Rayleigh numbers.

The second disconnected branch that we find in this range of Rayleigh numbers is branch (9) and arises at $Ra \approx 70000$ (see Fig. 12). From the bifurcation diagram of the kinetic energy (see Fig. 12(a)) we see that all the symmetries of the flow are broken in this branch and the flow pattern consists of a number of randomly oriented vortices. These flow structures are not persistent and hence the heat is not transferred effectively across the domain (see also Fig. 3(c)). Here, Fig. 12 shows that the potential energy of branch (9) increases along with the kinetic energy unlike in most of the other branches we considered and from Fig. 3(b) we see that it is significant in comparison to many other branches. Moreover, from the linear stability analysis of the perturbed steady states we find that both the upper and lower parts of this disconnected branch are stationary unstable, i.e. $\mathcal{R}(\lambda) > 0$ and $\mathcal{I}(\lambda) = 0$, with very large growth rates. This suggests that this branch is very unlikely to be observed in a laboratory experiment as it is very sensitive to finite perturbations and highlight the effectiveness of deflated continuation in identifying such unstable disconnected branches and steady-state solutions.

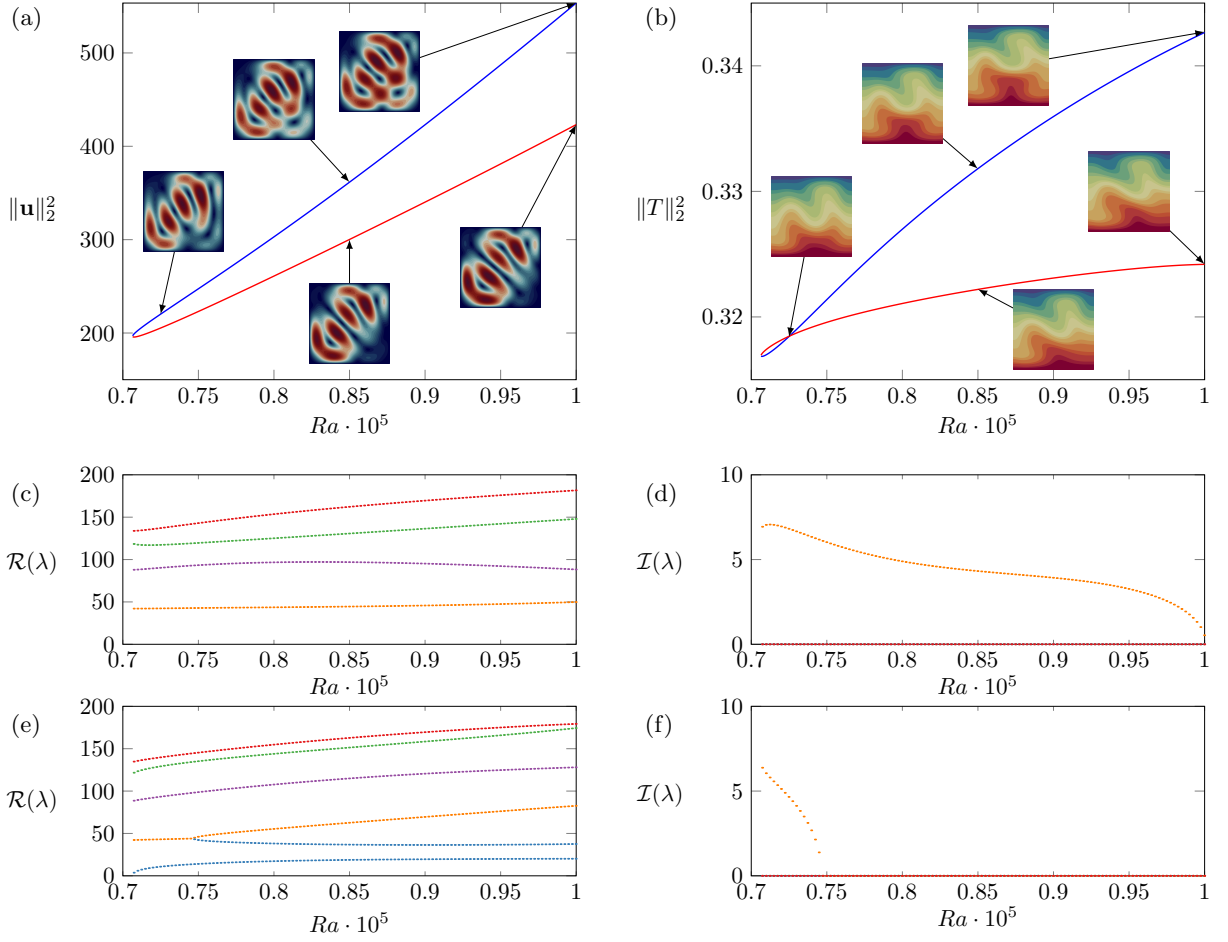


FIG. 12. (Color online) Evolution of the steady state flow patterns for (a) the kinetic energy and (b) the potential energy of the disconnected branch (9). The upper and lower parts of the branch are coloured in blue and red, respectively. The real and positive imaginary parts of the largest growth rates of the upper (resp. lower) part of the branch are presented in (c) and (b) (resp. (e) and (f)), respectively.

V. CONCLUSIONS

In this work, we have computed and analysed the linear stability of steady-state solutions of the two-dimensional Rayleigh–Bénard convection in a square cell with rigid walls. The combination of deflated continuation and a suitable initialization procedure based on the linear stability of the motionless state revealed to be a powerful numerical technique for finding multiple solutions including disconnected branches, which are not easily accessible by standard bifurcation techniques such as arclength continuation and time-evolution algorithms. A highlight is the success of deflation to discover these branches in an automated manner without any prior knowledge of the dynamics.

We classify the solutions based on the kinetic and potential energy as well as the Nusselt number. Our classification provides a clear view of the nonlinear dynamics of Rayleigh–Bénard convection up to a Rayleigh number of 10^5 . We show that the steady state solutions of branch (1) (which originates from the conducting state) dictate the dynamics of the flow for $Ra < 70000$, while for $70000 < Ra \leq 10^5$ the flow patterns of the disconnected branch (7) start to play a very important role. This is also indicated by the linear stability of solutions as Ra varies. Solutions on branch (7) are reminiscent of the flow pattern that plays the fundamental role in the turbulent dynamics of flow reversals that have been reported in the literature for Rayleigh–Bénard convection at $Ra \sim 10^7$ [29–31]. This disconnected branch exhibits a s-shape bifurcation with hysteresis which can be a challenge to discover with other bifurcation techniques.

There are several possible extensions to this work. An interesting but computationally challenging future study is to extend certain solutions of interest to higher values of Ra and determine whether they give the required theoretical scalings in the limit of high Rayleigh number. A first attempt toward this direction has been done in Rayleigh–Bénard convection with periodic boundary conditions in the horizontal direction and no-slip in the vertical direction [53, 54]. Moreover, the extensions of branch (7) and its stability in the regime where reversals occur is also of great interest.

Another extension of interest is to study how the states presented in this study change with respect to other parameters of the system such as the Prandtl number or the aspect ratio of the domain Γ . As observed in the left panel of Fig. 1, the critical Rayleigh number converges to $Ra_c^* \approx 1707.762$ for large aspect ratio. Using alternative formulations of the Rayleigh–Bénard problem, with the aspect ratio playing the role of the bifurcation parameter, it is possible to analyse the evolution of the branches for large aspect ratio and connect them with the solutions of the periodic set-up, which has been studied well in the literature, both analytically [41] and numerically [4, 5]. This connection will be of great interest to theoreticians and hopefully will spark their interest to explore analytical solutions on more realistic convection set-ups with spanwise walls.

A different future direction would be to perform bifurcation analysis on Rayleigh–Bénard convection in a three-dimensional rectangular domain. Such an approach will be of interest to experimentalists since direct comparisons with experiments would be possible. However, while the generalisation of the bifurcation technique employed in this paper to three dimensions is straightforward, high Rayleigh numbers require an efficient solver to perform the underlying Newton iterations. One possible solution would be to construct an efficient preconditioner robust with respect to the Rayleigh number to be able to reach high Ra regimes in the spirit of [55, 56].

ACKNOWLEDGMENTS

We would like to thank P. A. Gazca-Orozco and S. Fauve for helpful discussions that improved the quality of the manuscript. This work is supported by the EPSRC Centre For Doctoral Training in Industrially Focused Mathematical Modelling (EP/L015803/1) in collaboration with Simula Research Laboratory, and by EPSRC grants EP/V001493/1 and EP/R029423/1.

[1] M. C. Cross and P. C. Hohenberg, Pattern formation outside of equilibrium, *Rev. Mod. Phys.* **65**, 851 (1993).

[2] E. Bodenschatz, W. Pesch, and G. Ahlers, Recent developments in Rayleigh–Bénard convection, *Annu. Rev. Fluid Mech.* **32**, 709 (2000).

[3] N. Ouertatani, N. B. Cheikh, B. B. Beya, and T. Lili, Numerical simulation of two-dimensional Rayleigh–Bénard convection in an enclosure, *C. R. Mec.* **336**, 464 (2008).

[4] E. Zienicke, N. Seehafer, and F. Feudel, Bifurcations in two-dimensional Rayleigh–Bénard convection, *Phys. Rev. E* **57**, 428 (1998).

[5] S. Paul, M. K. Verma, P. Wahi, S. K. Reddy, and K. Kumar, Bifurcation analysis of the flow patterns in two-dimensional Rayleigh–Bénard convection, *Int. J. Bifurcat. Chaos* **22**, 1230018 (2012).

[6] P. K. Mishra, P. Wahi, and M. K. Verma, Patterns and bifurcations in low–Prandtl-number Rayleigh–Bénard convection, *EPL* **89**, 44003 (2010).

[7] J. W. Peterson, *Parallel adaptive finite element methods for problems in natural convection*, Ph.D. thesis, University of Texas, Austin (2008).

[8] H. B. Keller, Numerical solution of bifurcation and nonlinear eigenvalue problems., in *Applications of Bifurcation Theory* (Academic Press, 1977) pp. 359–384.

[9] D.-J. Ma, D.-J. Sun, and X.-Y. Yin, Multiplicity of steady states in cylindrical Rayleigh–Bénard convection, *Phys. Rev. E* **74**, 037302 (2006).

[10] K. Borońska and L. S. Tuckerman, Extreme multiplicity in cylindrical Rayleigh–Bénard convection. I. Time dependence and oscillations, *Phys. Rev. E* **81**, 036320 (2010).

[11] K. Borońska and L. S. Tuckerman, Extreme multiplicity in cylindrical Rayleigh–Bénard convection. II. Bifurcation diagram and symmetry classification, *Phys. Rev. E* **81**, 036321 (2010).

[12] W. E. Arnoldi, The principle of minimized iterations in the solution of the matrix eigenvalue problem, *Q. Appl. Math.* **9**, 17 (1951).

[13] D. Puigjaner, J. Herrero, F. Giralt, and C. Simó, Stability analysis of the flow in a cubical cavity heated from below, *Phys. Fluids* **16**, 3639 (2004).

[14] D. Puigjaner, J. Herrero, F. Giralt, and C. Simó, Bifurcation analysis of multiple steady flow patterns for Rayleigh–Bénard convection in a cubical cavity at $Pr = 130$, *Phys. Rev. E* **73**, 046304 (2006).

[15] E. J. Doedel, AUTO: A program for the automatic bifurcation analysis of autonomous systems, *Congr. Numer.* **30**, 25 (1981).

[16] H. Uecker, D. Wetzel, and J. D. M. Rademacher, pde2path-A Matlab package for continuation and bifurcation in 2D elliptic systems, *Numer. Math.-Theory Me.* **7**, 58 (2014).

[17] H. A. Dijkstra, F. W. Wubs, A. K. Cliffe, E. Doedel, I. F. Dragomirescu, B. Eckhardt, A. Y. Gelfgat, A. L. Hazel, V. Lucarini, A. G. Salinger, *et al.*, Numerical Bifurcation Methods and their Application to Fluid Dynamics: Analysis beyond Simulation, *Commun. Comput. Phys.* **15**, 1 (2014).

- [18] L. S. Tuckerman and D. Barkley, Bifurcation analysis for timesteppers, in *Numerical methods for bifurcation problems and large-scale dynamical systems* (Springer, 2000) pp. 453–466.
- [19] C. K. Mamun and L. S. Tuckerman, Asymmetry and Hopf bifurcation in spherical Couette flow, *Phys. Fluids* **7**, 80 (1995).
- [20] P. E. Farrell, A. Birkisson, and S. W. Funke, Deflation techniques for finding distinct solutions of nonlinear partial differential equations, *SIAM J. Sci. Comput.* **37**, A2026 (2015).
- [21] P. E. Farrell, C. H. Beentjes, and Á. Birkisson, The computation of disconnected bifurcation diagrams, *arXiv preprint arXiv:1603.00809* (2016).
- [22] S. J. Chapman and P. E. Farrell, Analysis of Carrier’s problem, *SIAM J. Appl. Math.* **77**, 924 (2017).
- [23] D. B. Emerson, P. E. Farrell, J. H. Adler, S. P. MacLachlan, and T. J. Atherton, Computing equilibrium states of cholesteric liquid crystals in elliptical channels with deflation algorithms, *Liquid Crystals* **45**, 341 (2018).
- [24] E. G. Charalampidis, P. G. Kevrekidis, and P. E. Farrell, Computing stationary solutions of the two-dimensional Gross–Pitaevskii equation with deflated continuation, *Commun. Nonlinear Sci. Numer. Simulat.* **54**, 482 (2018).
- [25] E. G. Charalampidis, N. Boullé, P. G. Kevrekidis, and P. E. Farrell, Bifurcation analysis of stationary solutions of two-dimensional coupled Gross–Pitaevskii equations using deflated continuation, *Commun. Nonlinear Sci. Numer. Simulat.* **87**, 105255 (2020).
- [26] N. Boullé, E. G. Charalampidis, P. E. Farrell, and P. G. Kevrekidis, Deflation-based identification of nonlinear excitations of the three-dimensional Gross–Pitaevskii equation, *Phys. Rev. A* **102**, 053307 (2020).
- [27] S. Fauve, J. Herault, G. Michel, and F. Pétrelis, Instabilities on a turbulent background, *J. Stat. Mech. Theory Exp.* **2017**, 064001 (2017).
- [28] L. P. Kadanoff, *Statistical physics: statics, dynamics and renormalization* (World Scientific Publishing Company, 2000).
- [29] K. Sugiyama, R. Ni, R. J. Stevens, T. S. Chan, S.-Q. Zhou, H.-D. Xi, C. Sun, S. Grossmann, K.-Q. Xia, and D. Lohse, Flow reversals in thermally driven turbulence, *Phys. Rev. Lett.* **105**, 034503 (2010).
- [30] M. Chandra and M. K. Verma, Flow reversals in turbulent convection via vortex reconnections, *Phys. Rev. Lett.* **110**, 114503 (2013).
- [31] B. Podvin and A. Sergent, Precursor for wind reversal in a square Rayleigh–Bénard cell, *Phys. Rev. E* **95**, 013112 (2017).
- [32] H. Bénard, Etude expérimentale du mouvement des liquides propageant de la chaleur par convection. Régime permanent: tourbillons cellulaires, *C. r. hebd. séances Acad. sci. Paris* **130**, 1004 (1900).
- [33] L. Rayleigh, On convection currents in a horizontal layer of fluid, when the higher temperature is on the under side, *Phil. Mag. S.* **32**, 529 (1916).
- [34] H. Bénard, Sur les tourbillons cellulaires et la théorie de Rayleigh, *C. r. hebd. séances Acad. sci. Paris* **185**, 1109 (1927).
- [35] A. Oberbeck, Über die Wärmeleitung der Flüssigkeiten bei Berücksichtigung der Strömungen infolge von Temperaturdifferenzen, *Ann. Phys. Chem.* **243**, 271 (1879).
- [36] J. Boussinesq, *Théorie analytique de la chaleur mise en harmonic avec la thermodynamique et avec la théorie mécanique de la lumière*, Vol. II (Gauthier-Villars, 1903).
- [37] D. J. Tritton, *Physical fluid dynamics* (Springer, 2012).
- [38] F. Rathgeber, D. A. Ham, L. Mitchell, M. Lange, F. Luporini, A. T. T. McRae, G.-T. Bercea, G. R. Markall, and P. H. J. Kelly, Firedrake: automating the finite element method by composing abstractions, *ACM Trans. Math. Softw.* **43**, 1 (2016).
- [39] G. W. Stewart, A Krylov–Schur algorithm for large eigenproblems, *SIAM J. Matrix Anal. A.* **23**, 601 (2002).
- [40] V. Hernandez, J. E. Roman, and V. Vidal, SLEPc: A scalable and flexible toolkit for the solution of eigenvalue problems, *ACM Trans. Math. Softw.* **31**, 351 (2005).
- [41] S. Chandrasekhar, *Hydrodynamic and Hydromagnetic Stability* (Oxford University Press, 1961).
- [42] P. Hirschberg and E. Knobloch, Mode interactions in large aspect ratio convection, *J. Nonlinear Sci.* **7**, 537 (1997).
- [43] S. Fauve, Henri Bénard and pattern-forming instabilities, *C. R. Phys.* **18**, 531 (2017).
- [44] J. Mizushima, Onset of the Thermal Convection in a Finite Two-Dimensional Box, *J. Phys. Soc. Japan* **64**, 2420 (1995).
- [45] E. D. Siggia, High Rayleigh number convection, *Annu. Rev. Fluid Mech.* **26**, 137 (1994).
- [46] Y. A. Kuznetsov, *Elements of applied bifurcation theory*, Vol. 112 (Springer Science & Business Media, 2013).
- [47] L. P. Kadanoff, Turbulent heat flow: structures and scaling, *Phys. Today* **54**, 34 (2001).
- [48] F. Ravelet, L. Marié, A. Chiffaudel, and F. Daviaud, Multistability and memory effect in a highly turbulent flow: Experimental evidence for a global bifurcation, *Phys. Rev. Lett.* **93**, 164501 (2004).
- [49] M. Berhanu, R. Monchaux, S. Fauve, N. Mordant, F. Pétrelis, A. Chiffaudel, F. Daviaud, B. Dubrulle, L. Marié, F. Ravelet, *et al.*, Magnetic field reversals in an experimental turbulent dynamo, *EPL-Europhys. Lett.* **77**, 59001 (2007).
- [50] O. Cadot, A. Evrard, and L. Pastur, Imperfect supercritical bifurcation in a three-dimensional turbulent wake, *Phys. Rev. E* **91**, 063005 (2015).
- [51] V. Dallas, K. Seshasayanan, and S. Fauve, Transitions between turbulent states in a two-dimensional shear flow, *Phys. Rev. Fluids* **5**, 084610 (2020).
- [52] P. Winchester, V. Dallas, and P. D. Howell, Zonal flow reversals in two-dimensional Rayleigh–Bénard convection, *arXiv preprint arXiv:2010.15642* (2020).
- [53] D. Sondak, L. M. Smith, and F. Waleffe, Optimal heat transport solutions for Rayleigh–Bénard convection, *J. Fluid Mech.* **784**, 565 (2015).
- [54] F. Waleffe, A. Boonkasame, and L. M. Smith, Heat transport by coherent Rayleigh–Bénard convection, *Phys. Fluids* **27**, 051702 (2015).
- [55] P. E. Farrell and P. A. Gazca-Orozco, An augmented Lagrangian preconditioner for implicitly-constituted non-Newtonian incompressible flow, *SIAM J. Sci. Comput.* **42**, B1329 (2020).

[56] P. E. Farrell, L. Mitchell, and F. Wechsung, An Augmented Lagrangian Preconditioner for the 3D Stationary Incompressible Navier–Stokes Equations at High Reynolds Number, *SIAM J. Sci. Comput.* **41**, A3073 (2019).